J. Min. Metall. Sect. B-Metall. 49 (3) B (2013) 315 - 322

Journal of Mining and Metallurgy, Section B: Metallurgy

RELATIONSHIP BETWEEN COOLING RATE AND MICROSEGREGATION IN BOTTOM-CHILLED DIRECTIONALLY SOLIDIFIED DUCTILE IRONS

W.S. Chang[a], C.M. Lin[a, b, *]

[a] Department of Mechanical Engineering, National Taiwan University of Science and Technology, Taipei, Taiwan

[b] Ira A. Fulton Schools of Engineering, Arizona State University, Tempe, United States

(Received 02 July 2012; accepted 08 July 2013)

Abstract

This study explores the relationship between cooling rate and microsegregation of directionally solidified ductile iron. The unidirectional heat transfer system used in this research is made up of a copper mold kept chilled by circulating water and embedded in the bottom of Furan sand mold. Thermocouples are connected to the computer measuring system to record the cooling curves of the castings at a distance of 0, 30, 60 and 90 mm from the chilled copper mold surface. Alloys including Mn, Cr, Cu, Ni and Ti were added to the specimens. Electron microprobe analysis (EPMA) was employed to examine distribution of elements between the dendrite arms and nodular graphite. Results show that unidirectional heat transfer affects directly the solidification mode and microstructure of the casting. The cooling curves reveal that local solidification time increases with increasing distance from the chilled copper mold surface. Different solidification rates with corresponding microstructure and element segregation were observed in the same unidirectionally solidified casting. Local solidification time was closely related to element segregation. The effective segregation coefficient (K_{eff}) calculated using the Scheil equation was found to vary, according to the stage of solidification. The actual segregation characteristics of complex alloys generally follow the Scheil equation.

Keywords: *Directionally solidified; Micro segregation; Ductile iron*

1. Introduction

Factors affecting the mechanical properties and microstructure of ductile iron include the cooling rate during solidification, the chemical composition of ductile iron and the casting procedures. Prior to the solidification of ductile iron, the inoculation process causes nucleation of nodular graphite in the molten iron. When the temperature drops to the eutectic temperature range, the duration of local solidification will determine both the quantity and dimensions of graphite formed [1]. In addition, the distribution and redistribution of solute during alloy solidification is also related to the local solidification time and half-width of dendrite arms [2,3]. For heavy-section metal castings, prolonged local solidification time will cause graphite degeneration or flotation. Moreover, segregation of alloys will become more serious and macrosegregation will occur, resulting in low yield rate [4,5]. Using thermal analysis to study the release of latent heat, changes in solid fraction and alloy segregation during cast solidification can contribute to the prediction and control of the microstructure of cast iron [6-12].

When castings are cooled, the release of latent heat will lead to changes in the cooling curve. Changes in slope of temperature against time as observed on a differential cooling curve are indicative of characteristic temperatures at which austenite liquidus arrest occurs, and at the beginning and end of eutectic temperature. Stefanescu et al.[11] proposed using zero-curve calculations to examine the relationship between the morphology of graphite and the latent heat released during the transformation from liquid to solid phase. In their calculations, the total value of latent heat released during cast solidification is denoted by the area enclosed within the zero curve and differential cooling curve, as expressed by the following equations[6]:

$$\frac{dQ_L}{dt} = -V\rho C_P\left[(\frac{dT}{dt})_{CC} - (\frac{dT}{dt})_{ZC}\right] \quad \ldots(1)$$

where $(\frac{dT}{dt})_{ZC}$ is the area enclosed within the zero curve, $(\frac{dT}{dt})_{CC}$ is the differential cooling curve (cooling rate), V is the volume of the section, ρ is the density,

* *Corresponding author: clin112@asu.edu*

DOI:10.2298/JMMB120702034C

Cp is the heat capacity, Q_L is the heat of solidification, and t is the time.

Following the approach proposed by Stefanescu et al. [11], the total latent heat released at the end of eutectic transformation and at the beginning of eutectoid transformation can be obtained. The best value to be chosen from the area obtained should be as close as possible to the beginning of eutectoid transformation and as far as possible from the end of eutectic transformation. In order that the value of latent heat released during solidification of heavy-section castings fits better the solid-phase first derivative curve, the interaction between the zero curve and liquid-phase first derivative curve will be shifted. Such change in heavy-section castings cannot be neglected; otherwise, the latent heat calculated will be smaller than the actual value [6, 7]. According to the Newtonian Thermal Analysis Theory, the solid fraction can be calculated from the changes in latent heat released with time using the following equation:

$$f_s(t) = \frac{1}{L}\int_{t_{AL}}^{t_E} Q_L(t)dt \quad \ldots(2)$$

where f_s is the solid fraction, L is the total latent heat released, t_{AL} is the time at which austenite liquidus arrest occurs, and t_E is the time when eutectic transformation ends [8-10].

Computer-aided thermal analysis of the first derivative curve can clearly reveal the impact of different characteristic temperatures during phase transformation on cast solidification. Early research has already used changes in curvature of cooling curves to identify the different phases of eutectic transformation during cast solidification, and the structure of cooling curves to determine the nodularity and morphology of graphite in cast irons [11]. With advances in computer-aided thermal analysis, more recent studies were able to observe even the less obvious physical significance of cooling curves. Take for instance the differential cooling curves of ductile iron with eutectic composition C.E.£ 4.6%. The presence of magnesium suppresses the formation of graphite. Hence, characteristic temperatures for liquidus austenite and nodular graphite can both be observed during initial solidification. In addition, changes in latent heat released by both graphite and austenite in the eutectic region of the first derivative curve can help predict the quality of nodular graphite. In the case of pearlitic ductile iron, not all carbon is transformed into graphite during solidification. Incomplete releases of latent heat led to fluctuations are observed in the eutectic region of the first derivative curve [12, 13].

Elements including Mn, Cu, Ni, Cr and M are added when casting ductile iron to enhance its mechanical properties. However, non-equilibrium solidification will cause uneven distribution of elements, resulting in segregation. In particular, a high concentration of carbide promoters including Mn, Cr and Mo in the solid solution of the matrix will result in formation of interdendritic carbides in granular, platy, blocky and even network shape. Excessive interdendritic carbides in the casting will deteriorate its mechanical properties, and sometimes the deterioration is so bad that the casting cannot be used. Carbide-promoting elements not only affect the solidified iron, but they also influence each other. Moreover, local solidification time is related to solute redistribution and coarsening of dendrite arms and eutectic cells. Hence, while the microstructure of castings is affected by the alloy elements added, the cooling rate is the key determinant [14-18]. According to Scheil equation, dendrite structure is formed at a small ratio of temperature gradient to solidification rate, as expressed by G/R where G denotes temperature gradient and R stands for growth velocity. Hence, when exploring growth of dendrite and solute redistribution, the Scheil equation can be rewritten as

$$C_s^* = kC_0(1-f_s)^{k-1} \quad \ldots(3)$$

where C_s^* is the solute concentration at solid/liquid interface, C_0 is the average solute concentration of dendrite, k is the segregation coefficient, and f_s is the solid fraction.

In addition, graphite is already formed during initial solidification; hence, the effect of nodular graphite on segregation of alloy elements is less obvious[19]. In this study, both graphite-promoting elements including Si, Cu and Ni and carbide-promoting elements including Mn, Cr and Ti are added to heavy-section ductile iron of dimensions 110 mm x 110 mm x 160 mm. The specimens are unidirectionally solidified. Cooling curves of cast iron specimens at different distance from the chilled copper mold surface are examined to shed light on the relationship between cooling rate and segregation of elements in the microstructure.

2. Experimental Design

2.1. Raw materials

Raw materials including pig iron, silicon steel and ferrosilicon, nodulizer containing 5% Mg, ferromanganese and other alloy elements, such as Mn, Cr, Cu and Ni, were first melted in a high-frequency induction furnace. The iron melt was nodularized using sandwiched method for nodularization and then poured in the Furan sand mold which the copper mold embedded in the bottom of Furan sand mold and kept chilled by circulating water. The top of the casting was sealed with exothermic compound (Foseco) for thermal insulation; hence, heat flux was only removed at the bottom by the copper mold kept chilled with circulating water. Table 1 lists the chemical

compositions of the two castings studied. As can be seen, the two castings comprise the same alloy elements. In comparison, Casting A contains greater concentration of Mn and Cr than Casting B while Casting B contains more Cu, Ni and Ti.

Table 1. *Chemical compositions of unidirectionally solidified ductile iron castings.*

	C.E(%)	Elements (wt%)								
		C	Si	Mn	Cr	Cu	Ni	Ti	Mg	Fe
A	4.56	3.7	2.57	0.51	0.61	0.01	0.02	0.03	0.05	bal.
B	4.01	3.12	2.66	0.05	0.05	0.7	0.7	0.12	0.04	bal.

2.2. Temperature measurement system

Figure 1 is the schematic diagram of the measuring system and water-chilled copper mold. As can be seen, the measuring system comprises four K-type thermocouples, a transmitter with a PCL 818H card, and a personal computer. The K-type thermocouples of 3.2 mm diameter were embedded inside each of the casting molds and placed at four different positions labeled as TC1, TC2, TC3 and TC4. As can be seen, these positions are at equal distance of 30 mm apart and at increasing distance (0, 30, 60 and 90 mm) from the bottom of the casting which is in contact with the chilled copper mold. The output voltage of the thermocouples were recorded by the transmitter and read by an external A/D card (PCL 818H, Advantech Co. Ltd., Taiwan) using the GENIE software. The voltage read was converted into solidification temperature and recorded once every sec throughout the process. Temperature records thus obtained were then employed to plot the cooling curves of the solidification process.

2.3. Microstructure and quantitative analysis

The two iron castings obtained by unidirectional solidification underwent grinding, polishing and etching. The microstructure of the two iron castings were then observed by scanning electron microscopy (SEM) at eight levels (L1-L8). These levels were at increasing distance from the chilled bottom of the castings, each at an interval of 17 mm. Elemental distribution in the spacing between dendrite arms and between nodular graphite were both determined using an electron microprobe analyzer (EPMA, JXA-8600SX).

3. Results and Discussion

3.1. Thermal analysis

As mentioned above, cooling curves reveal the changes in temperature from the liquid to solid phase with time. Figure 2 displays the cooling curves of the two castings. As can be seen, thermal arrest is observed for all cooling curves except that recorded at TC1. Thermal arrest occurs and remains constant during local solidification when the latent heat released and dissipated by both austenite and graphite during eutectic transformation is at equilibrium with the environmental heat flux. At position TC1, which is the bottom of the iron casting, the latent heat released was absorbed almost immediately by the chilled copper mold; hence, no thermal arrest was observed. As seen in the figure, the thermal arrest region of both castings are observed at TC4. In addition, the region of thermal arrest for Castings A and B shows different characteristics. Comparatively, the cooling curve of Casting B shows a shorter thermal arrest. With decrease in eutectic temperature with time, no obvious thermal arrest is observed. Such phenomenon

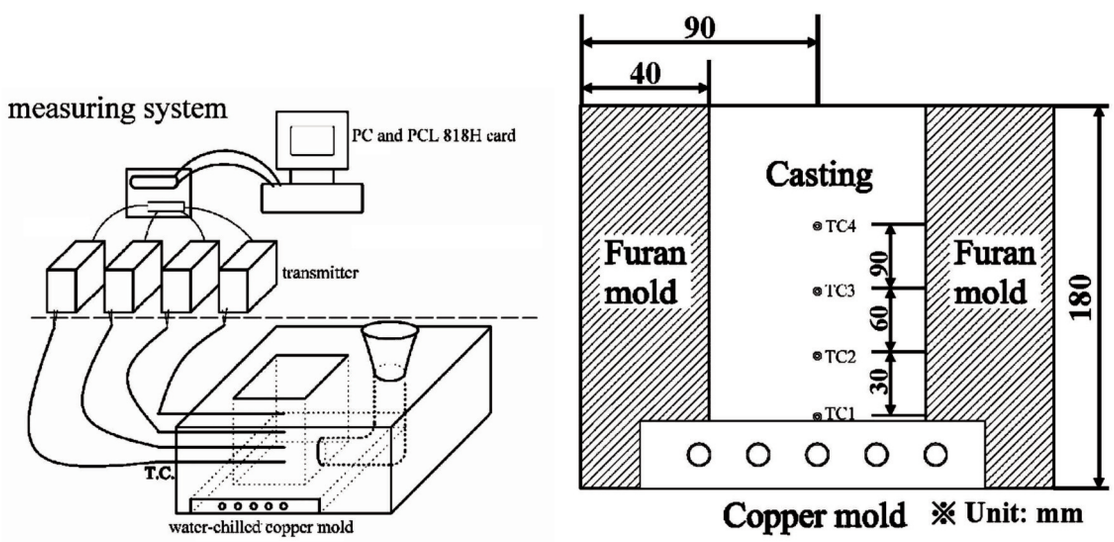

Figure 1. *Temperature measuring system and casting mold for directional solidification.*

can be attributed to the unstable growth of graphite toward the end of solidification. The morphology of graphite is a possible reason accounting for the decrease in temperature of thermal arrest, which has a significant effect on the nodularity of cast iron. Hence, the microstructure of the solidified ductile iron can be predicted by simply referring to its cooling curves.

3.2. Metallographical microstructure analysis

Figure 3 displays SEM images of Castings A and B showing changes in metallographical microstructure at various levels from the chilled bottom. Directional morphology can be observed and the metallographical microstructures formed evidence reverse of heat transfer. At L1 of both castings, which are in direct contact of the chilled copper mold, strips of ferrite in the matrix are seen. In Casting A, the nodular graphite increases in size with increasing distance from the chilled copper mold. In contrast, the nodular graphite at L4 becomes completely surrounded by ferrite in the pearlitic matrix, showing a bull-eye structure. Further away from the chilled casting bottom, the nodular graphite shows changes in appearance. At L6, segregation of alloys become more obvious with network carbides existing between dendrites and chunky graphite formed in the matrix. The dimensions of graphite change according to the direction of solidification, and the size of the graphite formed increases with increasing distance from the chilled mold. At L8, complete nodular graphite can no longer be seen. Instead, exploded graphite or floated graphite surrounded by graphite flakes is observed. The degeneration and floatation of graphite are mainly attributed to prolonged local solidification time [5].

Nucleation of inoculated ductile iron begins during the liquid phase with main growth occurring during eutectic transformation. From the cooling curve of Casting A shown in Figure 2, the local solidification time, t_f, for positions TC3 and TC4 are 660 sec and 1050 sec, respectively. These two positions correspond to L4 and L6 of Casting A, respectively. As seen in the metallographical microstructure of Casting A, interdendritic carbides are formed under segregation of carbide-promoting elements at local solidification time exceeding that at L4 (660 sec). In addition, graphite degeneration and floatation occur at local solidification time longer than that at L6 (1050 sec).

Despite undergoing the same solidification process, Castings A and B show different metallographical microstructures and morphologies of nodular graphite in the matrix. For instance, graphite degeneration of Casting B occurs much earlier at L4. The differences observed can be attributed to their variations in chemical composition. Although the same alloys are added, they are of different wt% in the two castings. As mentioned above, Casting B contains more Ti (0.12 wt%). When the liquid phase begins to solidify, the austenite shell surrounds the nodular graphite. However, the austenite boundaries are not completely sealed due to the presence of Ti compounds, thus providing a diffusion gallery for C to disperse. As a result, nodular graphite grows into compacted graphite or take the shape between nodular and compacted [20]. As seen in Figure 4(a), small particles (enclosed within the circle) are observed in the ferrite between graphite. SEM-EDS analysis revealed that these particles are TiC compounds. As seen in Figure 4(b) under 500 X magnification, pearlite is seen on both sides of the ferrite. Even before the transformation of austenite into pearlite, TiC already exists on the austenite boundary. The existence of TiC affects the diffusion of Carbon. As seen in the microstructure shown in Figure 4(a), the graphite in the lower part of the image is compacted under the influence of TiC.

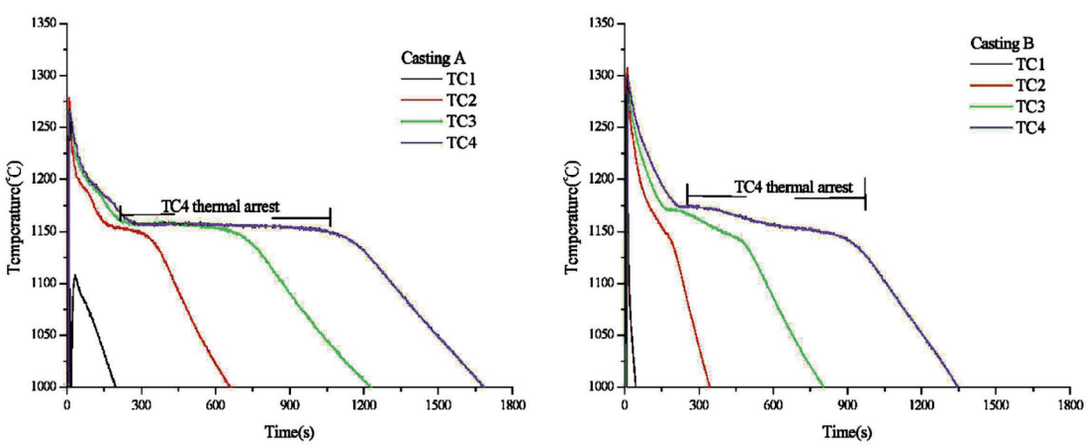

Figure 2. *Cooling curves of bottom-chilled directionally solidified Castings A and B.*

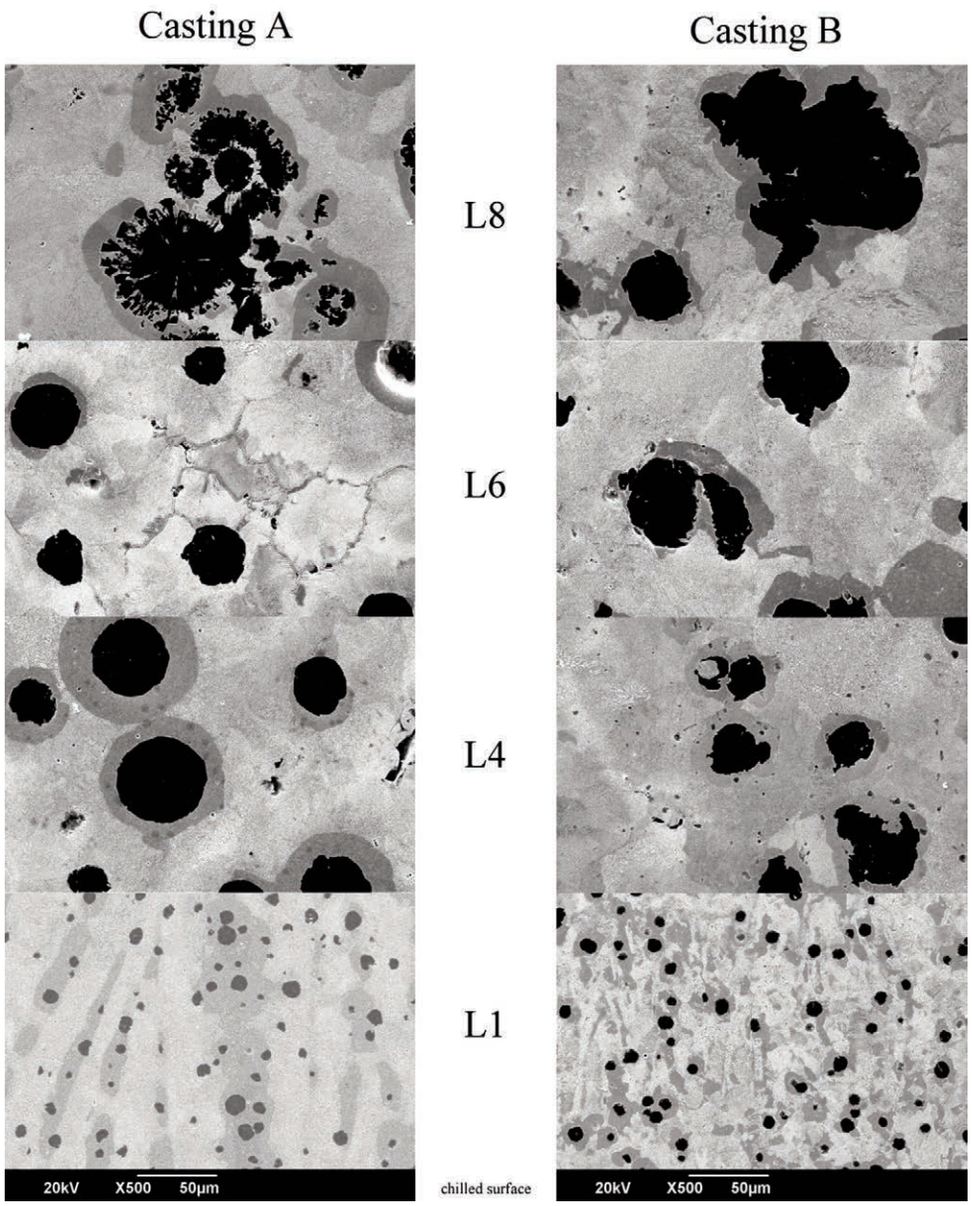

Figure 3. *SEM images of Castings A and B at various levels from chilled bottom (500 X magnification)*

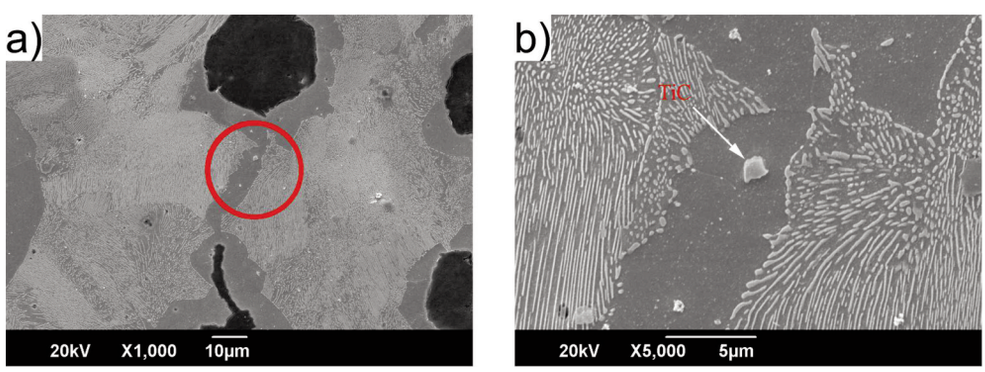

Figure 4. *Ti compounds formed on grain boundary of Casting B-L4*

3.3. Elemental distribution and theoretical calculation

Figure 5 presents EMPA results and SEM images of the two castings at L4. Point analysis was conducted from X to Y at an interval of 2 μm for Casting A and 5 μm for Casting B. The two castings present obvious differences in elemental composition and distribution.

In Casting A, dendrites formed during solidification of casting have enough time to grow and eventually become coarsened. Excessive solute is rejected into the liquid during solidificaiton, so high concentrations of Mn and Cr form rod-like interdendritic eutectic carbides in the final solidification zone, as seen in the SEM image of Casting A-L4 in Figure 5(a). At points X and Y, the elemental distribution of Casting A-L4 are similar, comprising roughly Si, 2.7 wt% ; Mn, 0.43 wt% ; and Cr, 0.32 wt%. However, there are wide variations within the spacing of dendritic arms. From point X, the concentration of both Mn and Cr first increase till 30 μm, then decrease and remain low till 80 μm. From there, they rise again, reaching their peaks around 90 μm and then drops till point Y. The concentration of Si shows exactly the opposite trend. In other words, when the Si content is at its highest, the Mn and Cr contents are at their lowest; and vice versa. These findings echo what has been mentioned earlier; that is, Si is a negative segregation elements of higher solute concentration in the initial solidification zone while Mn and Cr are positive segregation elements of higher interdendritic concentration. In addition, Mn and Cr are carbide-pormoting elements and may form eutectic carbides in the final solidification zone [14].

Casting B-L4 has differentelemental distribution as shown in Figure 5(b). It comprises Si, Ni and Cu, all reaching the highest concentrations of 2.79, 0.77 and 0.85 wt%, respectively at point Y. The variations in concentration of elements between points X and Y are not significant, except for Si, whose concentration drops to its lowest of 1.55 wt% at 20 μm from point X. As seen in the SEM image of Figure 5(b), point Y lies close to the nodular graphite. Formation of graphite has already begun in the initial solidification zone where the Si content is relatively higher. In the microstructure where

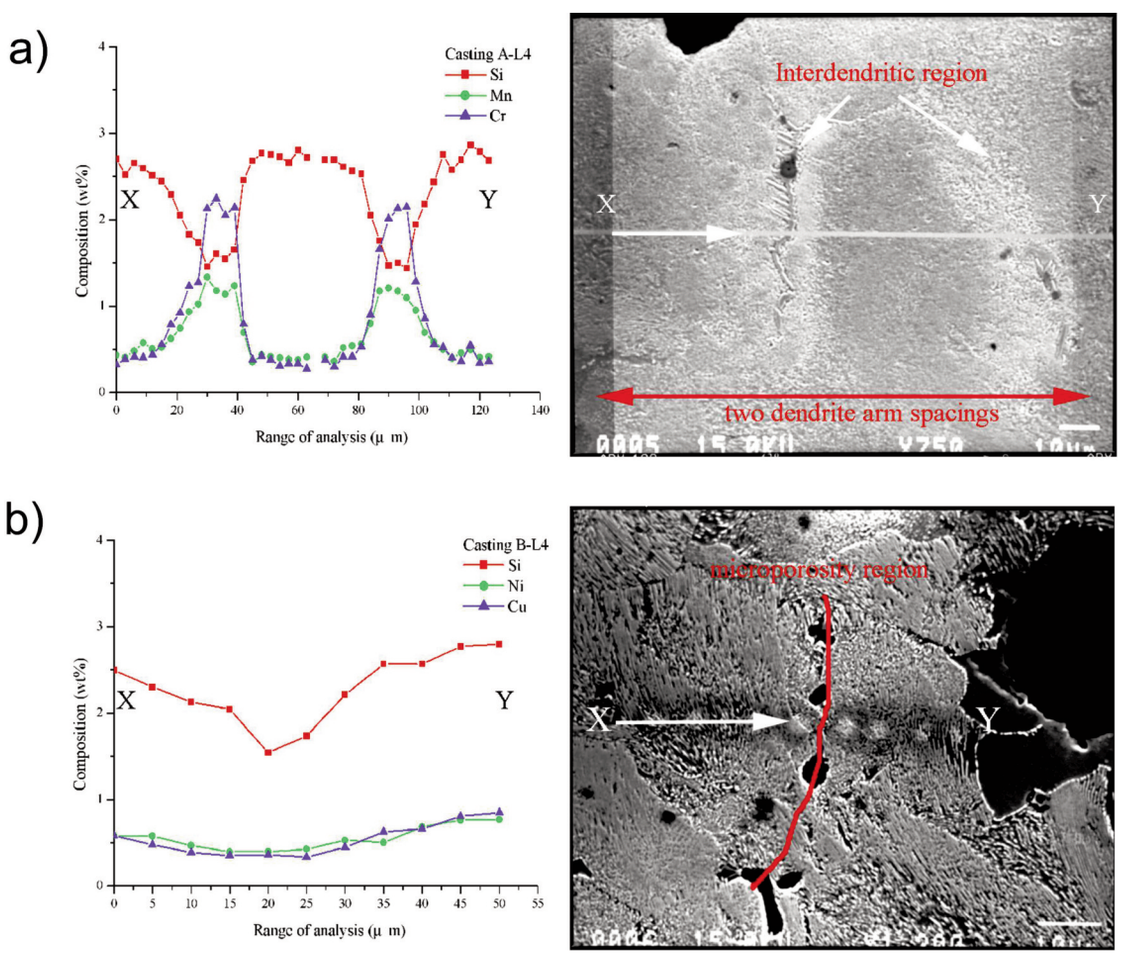

Figure 5. *(a) EMPA results and SEM image of Casting A-L4, (b) EMPA results and SEM image of Casting B-L4*

Si content is low, micro-porosity is observed, revealing it as the final solidification zone.

EMPA results and SEM images of metallographical microstructure can both shed light on the distribution of elements between dendrite arms and nodular graphite as well as the relationship between element segregation in the microstructure and non-equilibrium solidification. Full diffusion in liquid phase and limited diffusion in solid phase during non-equilibrium solidification will cause uneven distribution of elements, resulting in segregation. The degree of segregation is represented by the segregation coefficient, k, which is the ratio of solute concentration in the initial solidification zone to the average solute concentration [19]. As mentioned above, the effective segregation coefficient, K_{eff}, can be calculated by the Scheil equation $C_s^* = k_{eff} C_0 (1 - f_s)^{k_{eff}-1}$. Using the EMPA measured results, this study calculated the K_{eff} of L1-L8 and the average K_{eff} and the results thus obtained are listed in Table 2. In the calculation, the solute concentration of the initial solidification zone and the average solute concentration are substituted into C_S^* and C_0, respectively. Table 2 also shows the K_{eff} obtained in other studies [19]. As can be seen, our calculated results are consistent with those previously found.

Table 2. *Effective segregation coefficients (K_{eff}) obtained in this study and from references*

	A			B		
	Si	Mn	Cr	Si	Ni	Cu
L1	1.15	0.82	0.68	1.08	1.18	1.13
L2	1.08	0.73	0.64	-	-	-
L3	1.04	0.80	0.86	1.06	1.10	1.14
L4	1.05	0.83	0.68	1.21	1.32	1.46
L5	1.08	0.75	0.63	1.26	1.33	1.61
L6	1.02	1.05	1.07	1.20	1.40	1.56
L7	1.06	0.86	0.76	1.09	1.15	1.15
L8	1.00	0.74	0.71	1.33	1.29	1.31
Average	**1.06**	**0.82**	**0.75**	**1.20**	**1.27**	**1.39**
Ref. of effective segregation coefficients [19]						
Morita et al.	1.17	0.75	0.60	-	1.30	1.50
R. Boeri et al.	1.09	0.70	0.60	-	1.23	1.37
Kawawa et al.	1.50	0.70	0.50	-	1.40	-

Figure 6 displays the EMPA measurements and the calculated solute distribution of the two castings at L4. C_0 is the average EMPA results. As seen in Figure 6(a), at solid fraction between 0 and 60%, the calculated and experimental results follow the same trend; that is, Si content decreases while both Mn and Cr contents increase with increasing solid fraction. Such findings echo the trends of initial solidification shown in Figure 5(a). In addition, the measured and calculated values are close at solid faction of 0-60%. However, greater deviation in their values are observed when solid fraction exceeds 60%, with Si content measured lower than the calculated value and both Mn and Cr contents measured higher than the calculated ones. Such discrepancy is attributed to the formation of interdendritic eutectic carbides in the final solidification zone, as observed in the SEM image of Figure 5(a). Similarly, the calculated and experimental solute distributions shown in Figure 6(b) follow the same trend; that is, the larger the solid faction, the lower the Si, Ni and Cu contents. Moreover, the two values show no significant difference at all solid factions. The close resemblance in calculated and experimental solute distributions for Casting B can be attributed to the absence of interdendritic eutectic carbides formed, as seen in the SEM image of Figure 5(b). Although there is micro-porosity observed, it does not affect solute redistribution.

According to the theoretical analysis of elemental segregation, the effective segregation coefficient of the elements govern their distributions in the matrix throughout the solidification process. Nevertheless, in the actual solidification process, austenite and graphite are formed simultaneously with excess solute released in the liquid phase. Both Mn and Cr are carbide-promoting elements; hence, high concentrations of Mn and Cr will cause eutectic carbides to be formed in the final solidification zone, as observed in the SEM image of Casting A-L4 in Figure 5(a). Carbides contain high concentration of alloy elements, thus raising the EMPA values at larger solid fraction, as evidenced by the higher EMPA values of Mn and Cr compared with the calculated ones. In sum, without eutectic carbides formed in the matrix, the effective segregation coefficient obtained by calculation are accurate representation of the actual elemental segregation. On the contrary, in the presence of interdendritic carbides eutectic formed, the EMPA values of carbide-promoting elements in the final solidification zone will be higher than those calculated using the Scheil equation. Hence, the segregation characteristics of complex alloys in general follow the Scheil equation.

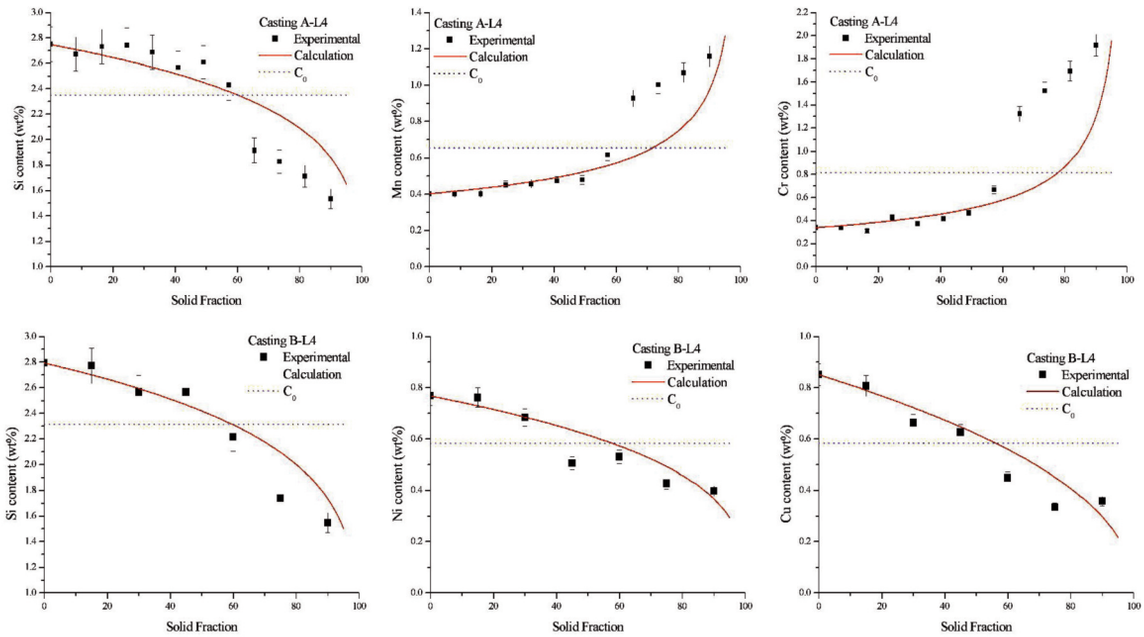

Figure 6. *(a) Experimental and calculated results of solute distribution of Casting A-L4, (b) Experimental and calculated results of solute distribution of Casting B-L4*

4. Conclusions

This study explores the relationship between cooling rate and microsegregation of directionally solidified ductile iron. The following conclusions are drawn from the experimental results.

The cooling curves reveal that local solidification time increases with increasing distance of the casting from the chilled copper mold surface. Besides the alloys added, local solidification time is another key determinant of the microstructure of castings and affects element segregation.

Under the influence of unidirectional heat transfer, the microstructure of unidirectionally solidified cast iron shows growth, degeneration and floatation of graphite, element segregation, and formation of carbides.

In terms of solute distribution, negative segregation elements including Si, Cu and Ni are of higher concentrations in the initial solidification zone while positive segregation elements including Cr and Mn are of higher concentrations in the final solidification zone. In addition, eutectic carbides are formed under higher contents of Cr and Mn. In general, the segregation characteristics of complex alloys follow the Scheil equation.

References

[1] T. Skaland, Ø. Grong, AFS trans., 99 (1991) 153-157.

[2] Harold D. Brody, Merton C. Flemings, AIME, 236 (1966) 615-624.

[3] H. Yoo, R. Viskanta, Int. J. Heat Mass Transfer, 40 (1997) 3876-3882.

[4] A. Javaid, C. R. Loper, Jr., AFS trans., 103 (1995) 135-150.

[5] G. X. Sun, C. R. Loper, Jr., AFS trans., 91 (1983) 841-854 .

[6] I. G. Chen, D. M. Stefanescu, AFS trans., 92 (1984) 947-964.

[7] M. J. Oliveira, L. F. Malheiros, C. A. S. Ribeiro, JMPTec, 92 (1999) 25-30.

[8] K. G. Upadhya, D. M. Stefanescu, K. Lieu, and D. P. Yeager, AFS trans., 97 (1989) 61-66.

[9] E. Fras, W. Kapturkiewicz, A. Burbielko, H. F. Lopez, AFS trans., 101 (1993) 505-511.

[10] J. W. Gibbs, P. F. Mendez, Scirpta Materialia, 58 (2008) 699-702.

[11] D. M. Stefanescu, C. R. Loper, Jr., R. C. Voigt, and I. G. Chen, AFS trans., 90 (1982) 333-348.

[12] D. Emadi, L. V. Whiting, S. Nafisi and R. Ghomashchi, J. Therm. Anal. Calorim., 81 (2005) 235-242.

[13] David Sparkman, “Ductile Iron Microstructure by Thermal Analysis”, web: http://www.meltlab.com/index.php, 2008.

[14] P. C. Liu, C. R. Loper, Jr., AFS trans., 89 (1981) 131-140.

[15] M. M. Shea, AFS trans., 86 (1978) 7-12.

[16] S. K. Yu, and C. R. Loper Jr., AFS trans., 96 (1988) 811-822.

[17] D. Venugopalan, A. Alagarsamy, AFS trans., 98 (1990) 395-400.

[18] T. F. Bower, H. D. Brody, and M. C. Flemings, AIME, 236 (1966) 624-634.

[19] R. Boeri, F. Weinberg, AFS trans., 97 (1989) 179-184.

[20] Yih-Hun Shy, Cheng-Hsun Hsu, Shen-Chih Lee, and Chih-Yuan Hou, Materials Science and Engineering A, 278 (2000) 54-60.